Controllable transformation of sheet-like CoMo-hydro(oxide) and phosphide arrays on nickel foam as efficient catalysts for alkali water splitting and Zn–H_2O cell

P. Y', Y. Q., Y. Y., X. S.,
T. T. I.M', **, X. Y.', *

[a] G. K. L. L. C. E. M., S. I. C. P. S.,
G. N. U., G. I., 541004, C.
[b] G. K. L. I. M., S. I. M. S. E., G. I. U. El. T. I., G. I. 541004, C.
[c] S. A. B. I. C. (SABIC) K. A. U. S. T. I. (KAUST), T. I. 23955-6900, S. A.

HIGHLIGHTS

- $CoMoO_4$–$Co(OH)_2$ and CoMoP–CoP

GRAPHICAL ABSTRACT

K :
Sheet-like arrays
$CoMoO_4$–$Co(OH)_2$ (P)
Synergistic effect
Water splitting
Zn–H_2O cell

to drive 10 mA cm^{-2} and obtain robust high current stability at 500 mA cm^{-2} for 110 h with almost no attenuation. In addition, using CoMoP–CoP/NF as the cathode of a Zn–H_2O cell can provide a power density of 11.5 mW cm^{-2} and a stable 170 h for simultaneous H_2 and electricity generation. The excellent performance of the system is attributed to the unique sheet-like array morphology of combined catalysts providing large surface area and rich pore structure conducive to electrolyte diffusion and gas emission, as well as the synergies between the different components providing more catalytic active sites.

Introduction

In view of the serious carbon dioxide pollution caused by the excessive consumption of traditional fossil fuels, considerable efforts have been devoted to find clean and sustainable energy sources [1]. Hydrogen is deemed as an ideal sustainable chemical energy carrier, owing to its high energy density [2]. Electrochemical water splitting is generally regarded as prospective technologies for industrial-scale hydrogen production. Currently, Pt/C and RuO_2 noble catalysts have been considered as pioneering electrocatalytic hydrogen evolution reaction (HER) and oxygen evolution reaction (OER) catalysts [3,4], but their expensiveness and scarcity limit the industrial applications [5], prompting us to investigate non-noble metal catalysts. However, non-precious metal catalysts still require higher overpotential compared to precious metal-based catalysts, which unfortunately impedes large-scale hydrogen generation. Therefore, the development of low-cost and efficient transition metal-based catalysts is necessary for hydrogen production.

The state-of-the-art transition metals OER catalysts reported in the literature are based on Ni active sites that raise a severe environmental concern (Table S1) [6]. Cobalt hydroxide as an alternative is a reasonable OER electrocatalyst, which can serve as an alternative to RuO_2 due to its low cost and less environmental impact. However, its insufficient active surface and high charge transfer resistance can't significantly improve sluggish OER kinetics [7,8]. Based on this, doping with other transition metal compounds is an effective strategy for improving catalytic performance through a synergistic effect. Chen et al. [9] reported a hybrid composite of CoO_x-$CoMoO_4$ nanorod, which shows excellent OER performance due to the electron transfer between two components. Wang et al. [10] exhibited the hierarchical heterostructure CoP_3–$NiMoO_4$ nanosheets for overall water splitting on Ni foam. The HER performance originates from electronegativity of P atoms to capture positively charged protons [11]. Meanwhile, to meet the industrial requirements, the catalyst still faces severe challenges to continuously, rapidly and stably generate O_2 and H_2 at high current density (≥500 mA cm^{-2}) [12]. So the electrocatalysts required for overall water splitting still need to be further optimized through design strategies. The HER catalyst can serves as the cathode for Zn–H_2O cells that simultaneously generate electricity and hydrogen to reduce further the additional electricity required for overall water splitting [13]. While, the robust stability and mechanism of Zn–H_2O cell still need to be explored based on transition metal phosphides.

Herein, we reported a novel multifunctional $CoMoO_4$–$Co(OH)_2$/NF and CoMoP–CoP/NF combined catalysts that can be used for OER, HER, alkali water splitting and Zn–H_2O cell. The synthesis process of two hybrids is as follows, where the sheet-like ZIF-67 arrays were firstly synthesized on the surface of NF via dipping method. Then, the unstable ZIF-67 arrays in water were transformed into hierarchical $CoMoO_4$–$Co(OH)_2$ nanosheets by immersion etching method. Finally, it was further phosphated into CoMoP–CoP nanosheets. The microstructure, crystal structure, specific surface area, chemical state and composition of the $CoMoO_4$–$Co(OH)_2$/NF and CoMoP–CoP/NF hybrids have been systematically studied. Subsequently, we designed a system including "$CoMoO_4$–$Co(OH)_2$/NF had high OER activity, and CoMoP–CoP/NF showed better HER activity", and then their combination was used as high current alkali water splitting. Besides, the CoMoP–CoP/NF was also adopted as the cathode of alkaline Zn–H_2O cell, which could release H_2 and generate electricity at the same time. Most importantly, the optimized catalysts showed low overpotential and good stability at high current density (500 mA cm^{-2}), which is essential for industrial applications. In short, this work proposes a facile catalyst synthesis strategy that can be applied to both Zn–H_2O cell and alkali water splitting.

Experimental section

C M O_4–C $(OH)_2$/NF C $(OH)_2$/NF

ZIF-67/NF was fabricated by our reported work (detailed in supporting information) [14]. Then, Na_2MoO_4 (300 mg) was dissolved in 20 mL deionized water, and heated up to 80 °C. After that, ZIF-67/NF was fixed in the Na_2MoO_4 solution, gently stirred for 1 h. The resulted light blue sample was washed with deionized water, and dried at 60 °C, which was nominated as $CoMoO_4$–$Co(OH)_2$/NF. As a comparison, ZIF-67/NF was set in the deionized water, and stirred for 12 h. The light blue sample was rinsed and dried in the same conditions, and was designated as $Co(OH)_2$/NF. Moreover, RuO_2/NF was assembled by the reported method [14], the loading of RuO_2 was set to 2.0 mg cm^{-2} (detailed in supporting information).

to the following method: NaH_2PO_2 (0.7 g) was located at the intake side of the tube furnace, then $CoMoO_4$–$Co(OH)_2$/NF was located next to NaH_2PO_2 in direction of airflow. Then the temperature was rose from room temperature to 350 °C at 5 °C min^{-1}, and maintained for 3 h under Ar atmosphere. The resulted black sample was nominated as CoMoP–CoP/NF. As a comparison, CoP/NF was also prepared with $Co(OH)_2$/NF by the same phosphatization. Furthermore, Pt/C/NF was installed in the same method as RuO_2/NF, the loading of Pt/C were set to 1.0 mg cm^{-2}.

E

The electrocatalytic activity for OER and HER was estimated by the standard three-electrode mode of electrochemical workstation (Biologic VMP3) with 1.0 M KOH. The pH value of the 1.0 M KOH freshly prepared was 13.5 by pH meter and RHE voltage calibration in Fig. S1. The reference electrode and the counter electrode were saturated calomel electrode and carbon plate, respectively. The details were discussed in the supporting information (experimental section). For alkali water splitting, the performances were evaluated by two-electrode mode in 1.0 M KOH solution. The designed $CoMoO_4$–$Co(OH)_2$/$NF^{(+)}$ and CoMoP–CoP/$NF^{(-)}$ catalyst acted as anode and cathode electrodes, respectively. Then, we continued to evaluate the catalysts in 30 wt% KOH solution that simulated industrial application conditions. We particularly explored the electrocatalytic activity and stability of the catalysts under high current density conditions. Aimed at alkaline Zn–H_2O cell, it was carried out in the mixture of 6.0 M KOH with 0.2 M $Zn(AC)_2$. Zn plate and CoMoP–CoP/NF were used as anode and cathode, respectively. The power density was calculated by the polarization curves, which performed by LSV method at 10 mV s^{-1}. The long-time durability was measured at 10 mA cm^{-2} using LAND testing system.

Results and discussion

I - .

The $CoMoO_4$–$Co(OH)_2$/NF and CoMoP–CoP/NF were finely designed through ZIF-67 - . conversion and phosphating procedure in Fig. 1a. Sheet-like ZIF-67 is evenly self-assembled on the surface of NF by dipping process [14]. Fig. S2 shows the characteristic peaks of ZIF-67 crystal that match previously published ZIF-67 [15,16]. ZIFs crystal is synthesized via the coordination of metal ions and imidazolate ligands [17]. Previous reports demonstrate that ZIF-67 is unstable in water and etched into released Co^{2+} ions [18]. ZIF-67 could be transformed into light blue $CoMoO_4$–$Co(OH)_2$ via dipping in $NaMoO_4$ water solution (Fig. S3a), and the quantitative ratio between $Co(OH)_2$ and $CoMoO_4$ was calculated as 3.4:1 (Table S2). Then, $CoMoO_4$–$Co(OH)_2$ was converted into black CoMoP–CoP during phosphating. The loadings of $CoMoO_4$–$Co(OH)_2$ and CoMoP–CoP were respectively 6.9 and 7.3 mg cm^{-2}.

Fig. 1a and b illustrate the X-ray powder diffraction (XRD) patterns of $CoMoO_4$–$Co(OH)_2$ and CoMoP–CoP, together with $Co(OH)_2$ and CoP as comparative catalysts. The diffraction peaks at 11.5°, 23.2°, 34.5° and 59.8° can be indexed to the (003), (006), (102) and (110) planes of hexagonal $Co(OH)_2$ (JCPDS: 46-0605), respectively. The diffraction peaks at 23.3°, 27.5°, 32.9°, 36.8° and 48.8° can be corresponding to the (021), (−202), (−222), (400) and (−133) planes of monoclinic $CoMoO_4$ (JCPDS: 21-0868), respectively. This result explains that partial cobalt ions dissociated from ZIF-67 react with molybdate ions according to $MoO_4^{2-} + Co^{2+} = CoMoO_4\downarrow$, another part react with hydroxide ions to generate cobalt hydroxide according to the $2OH^- + Co^{2+} = Co(OH)_2\downarrow$, because the sodium molybdate solution is weak alkaline. XRD patterns of comparative

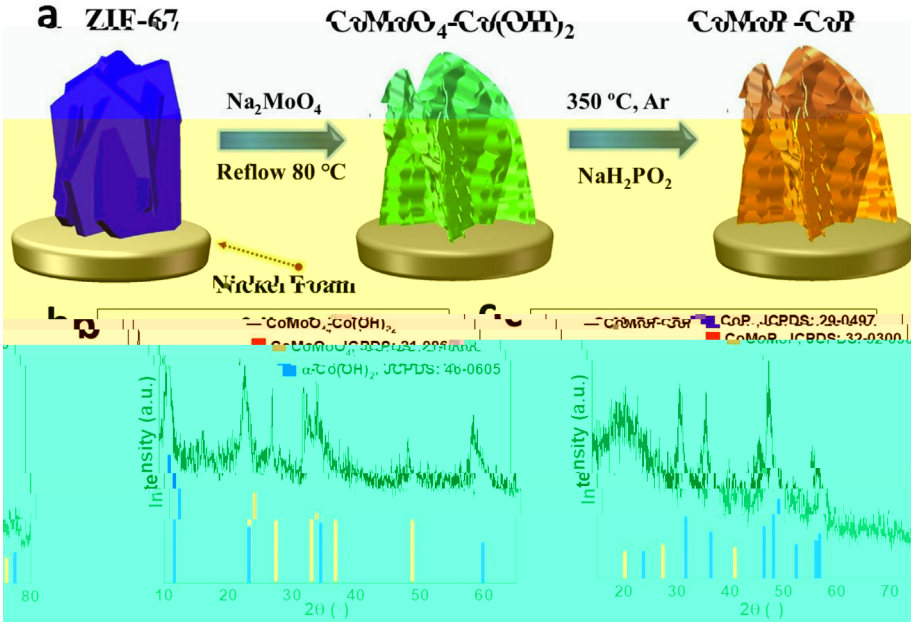

Fig. 1 – (a) The fabricating scheme of $CoMoO_4$–$Co(OH)_2$/NF and CoMoP–CoP/NF. XRD patterns of (b) $CoMoO_4$–$Co(OH)_2$ and (c) CoMoP–CoP.

$Co(OH)_2$ and CoP are the same as that of the corresponding substance in the $CoMoO_4$–$Co(OH)_2$ and CoMoP–CoP (Figs. S4a-b), implying that ZIF-67 in water is converted to $Co(OH)_2$, and then convert into CoP after phosphating.

M

The hierarchical and array structure of two catalysts was characterized by scanning electron microscopy (SEM). As shown in Fig. 2a, ZIF-67 is a smooth sheet with a thickness of ~154 nm. After ZIF-67 was transformed into $CoMoO_4$–$Co(OH)_2$, its smooth sheets convert into hierarchical sheets composed of many nanosheets (Fig. 2b). The CoMoP–CoP structure has little change during phosphating compared to $CoMoO_4$–$Co(OH)_2$ (Fig. 2c). Moreover, according to N_2 adsorption-desorption isotherm (Fig. 2d), they belong to typical type-III isotherm with the hysteresis loop. The specific surface area of CoMoP–CoP is 25.5 $m^2\ g^{-1}$, it is lower than $CoMoO_4$–$Co(OH)_2$ (51.6 $m^2\ g^{-1}$). The average gap sizes between the interwoven nanosheets of $CoMoO_4$–$Co(OH)_2$ and CoMoP–CoP are 25.5 and 23.6 nm, respectively, demonstrating a typical mesoporous material, which is beneficial to enhance gas emission and ion diffusion rate [19].

The TEM images reveal that $CoMoO_4$–$Co(OH)_2$ is composed by nanosheets (Fig. 3a), its 0.767 nm lattice spacing matches the (003) crystal plane of α-$Co(OH)_2$ (Fig. 3b). The SAED shows concentric diffraction rings consisting of discrete spots, which can be unambiguously assigned to the (110) plane of α-$Co(OH)_2$ and (−222) plane of $CoMoO_4$ (Fig. 3c). The high-angle annular dark field (HAADF) TEM elemental mappings in Fig. 3d demonstrate a uniform distribution of Co, Mo and O in $CoMoO_4$–$Co(OH)_2$ hybrid.

XPS

The XPS survey spectra of $CoMoO_4$–$Co(OH)_2$ and CoMoP–CoP display the co-existence of Co, Mo, O, P and C elements (Fig. S5a). As a calibration standard, we deconvolute the high resolution C 1 region into C=C (284.0 eV), C–C (284.8 eV) and C–N/C–O (286.0 eV) (Fig. S5b) [20]. In Fig. 4a, the Co 2 $_{3/2}$ spectrum of $Co(OH)_2$–$CoMoO_4$ displays two fitting peaks at 780.2 and 781.5 eV, belonging to Co^{2+} [2,21], the Co 2 $_{3/2}$ region for CoMoP–CoP shows two fitting peaks at 778.3 and 781.2 eV, they respectively match the cobalt phosphide and partial oxide [22,23]. As shown in Fig. 4b, the Mo 3 spectrum of $CoMoO_4$ respectively shows the spin orbit doublet Mo 3 $_{5/2}$ (231.5 eV) and Mo 3 $_{3/2}$ (234.7 eV) [24], the distance between the two peaks is 3.2 eV, this is the feature of the Mo^{6+} oxidation state [25]. The two peaks at 227.3 and 230.4 eV of Mo 3 are assigned to $Mo^{\delta+}$ species ($0 < \delta < 4$), other two doublets located at 234.9/231.8 eV and 233.1/230.0 eV are assigned to Mo^{6+} and Mo^{4+}, respectively, indicating the surface oxidation of CoMoP [26,27]. In the O 1 region of $CoMoO_4$–$Co(OH)_2$ (Fig. 4c), three binding energies of 530.0, 531.0 and 532.4 eV respectively correspond to the lattice oxygen, oxygen vacancies and absorbed oxygen species in the metal compounds [14,28]. According to Fig. 4d, in the P 2 region of CoMoP–CoP, the peak at 134.4 eV denotes the P–O binding energy because the phosphide surface is oxidized

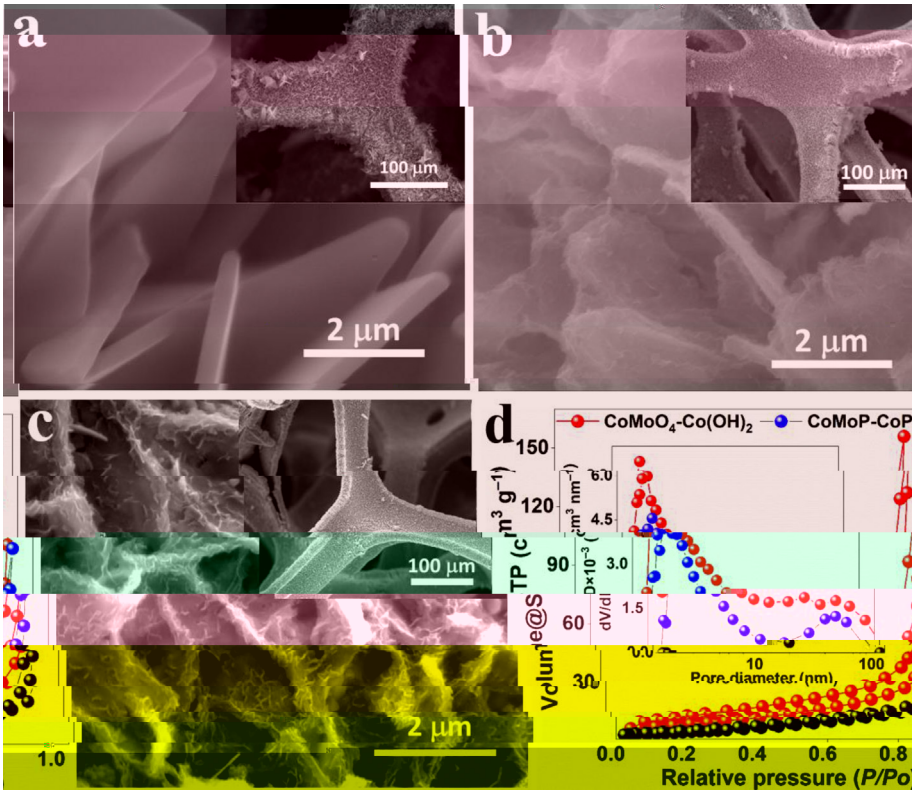

Fig. 2 – SEM images of (a) ZIF-67/NF, (b) $CoMoO_4$–$Co(OH)_2$/NF and (c) CoMoP–CoP/NF with different magnifications. (d) Nitrogen adsorption-desorption isotherms of $CoMoO_4$–$Co(OH)_2$ and CoMoP–CoP.

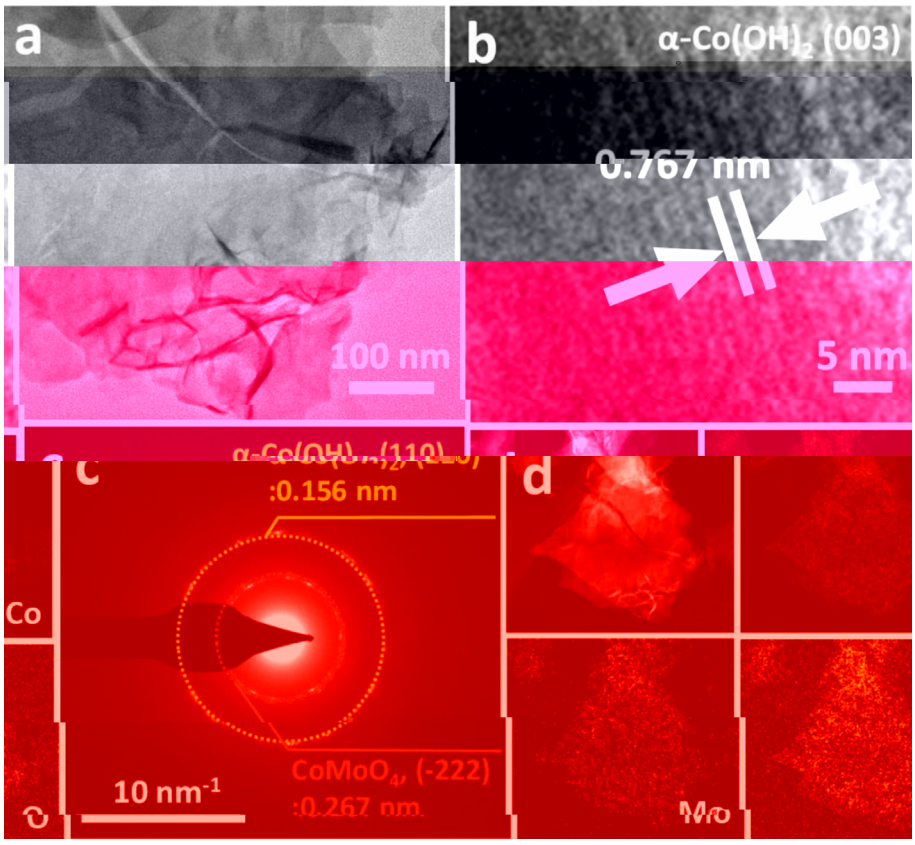

Fig. 3 – (a, b) TEM images of $CoMoO_4$–$Co(OH)_2$. (c) The corresponding selected area electron diffraction (SAED) images of $CoMoO_4$–$Co(OH)_2$. (d) Elemental mapping images of Co, Mo and O of $CoMoO_4$–$Co(OH)_2$.

[4], two fitting peaks at 130.0 (P 2 $_{3/2}$) and 130.9 eV (P 2 $_{1/2}$) are the binding energy of metal-P [29]. Notably, the Co $2p_{3/2}$ of $CoMoO_4$–$Co(OH)_2$ and CoMoP–CoP produces a negative shift of 0.42 and 0.24 eV relative to $Co(OH)_2$ and CoP, respectively (Figs. S6a-b), indicating the existence of strong electronic interactions between two components of two catalysts [30], which in turn facilitates charge transfer, thereby enhancing OER and HER performance [9,31].

OER HER

The OER performance of different catalysts are initially analyzed in alkaline media. According to Fig. 5a, the $CoMoO_4$–$Co(OH)_2$/NF presents a lower overpotential of 245.5 mV at 10 mA cm^{-2}, and outperforms those of RuO_2/NF (253.6 mV), CoMoP–CoP/NF (317.8 mV), and $Co(OH)_2$/NF (292.7 mV), respectively. Besides, the catalyst also exceeds most of the high-performance OER catalysts reported in the literature (Table S1) [9,10,32–45]. Since ZIF-67/NF cannot be converted to $CoMoO_4$/NF , we reference the literature for array-type $CoMoO_4$ (JCPDS: 21-0868) catalysts supported on nickel foam or carbon cloth, and the overpotentials were between 302 and 350 mV in Table S3. Particularly, the performance advantage is more prominent at higher current densities. The results imply a observable synergistic effect between Co and Mo species, namely the octahedral coordinated Co^{2+} in the $CoMoO_4$ is easier to oxidize to Co^{3+} in CoOOH, this evidently reinforces the electrochemical activity [42]. The $CoMoO_4$–$Co(OH)_2$/NF has the Tafel slope of 55.5 mV dec^{-1}, it is smaller than those of $Co(OH)_2$/NF (71.9 mV dec^{-1}) and RuO_2/NF (59.6 mV dec^{-1}) (Fig. 5b). In Fig. 5c, compared to the literatures of similar catalysts, $CoMoO_4$–$Co(OH)_2$/NF processes the lower values of the Tafel slope and overpotential, which indicate better catalytic kinetics of OER [46]. Many studies have found that the ECSA grows with the increasing electrochemical double layer capacitance (C_{dl}) [47]. In Fig. 5d and Fig. S7, the C_{dl} of $CoMoO_4$–$Co(OH)_2$/NF is 374.2 mF cm^{-2}, higher than those of $Co(OH)_2$/NF and RuO_2/NF, indicating its larger electrochemically active surface area [47]. The Nyquist plots are acquired by electrochemical impedance spectroscopy (EIS) [48]. As shown in Fig. S8a, the smaller semicircle diameter, the faster the charge transport rate of the electrode [49], $CoMoO_4$–$Co(OH)_2$/NF exhibits smaller semicircular diameter compared to $Co(OH)_2$/NF, implying that it has faster charge transfer ability. Furthermore, $CoMoO_4$–$Co(OH)_2$/NF can achieve a 0.01 s^{-1} turnover frequency (TOF) value at 313.3 mV overpotential (Fig. S9, Table S2), it is much lower than the 374.8 mV overpotential of $Co(OH)_2$/NF, revealing a better intrinsic activity of $CoMoO_4$–$Co(OH)_2$/NF [50].

The HER properties of different catalysts were evaluated via LSV in the three-electrode mode. The CoMoP–CoP/NF shows a lower 123.9 mV overpotential at 10 mA cm^{-2} in 1.0 M KOH, in comparison with CoP/NF (219.3 mV) and $CoMoO_4$–$Co(OH)_2$/NF (237.1 mV) (Fig. S10a). According to Fig. S10b, CoMoP–CoP/NF has the Tafel slope of 62.5 mV dec^{-1}, it is less than those of CoP/NF (114.6 mV dec^{-1}) and $CoMoO_4$–$Co(OH)_2$/NF (196.9 mV dec^{-1}), this result reveals that the HER of

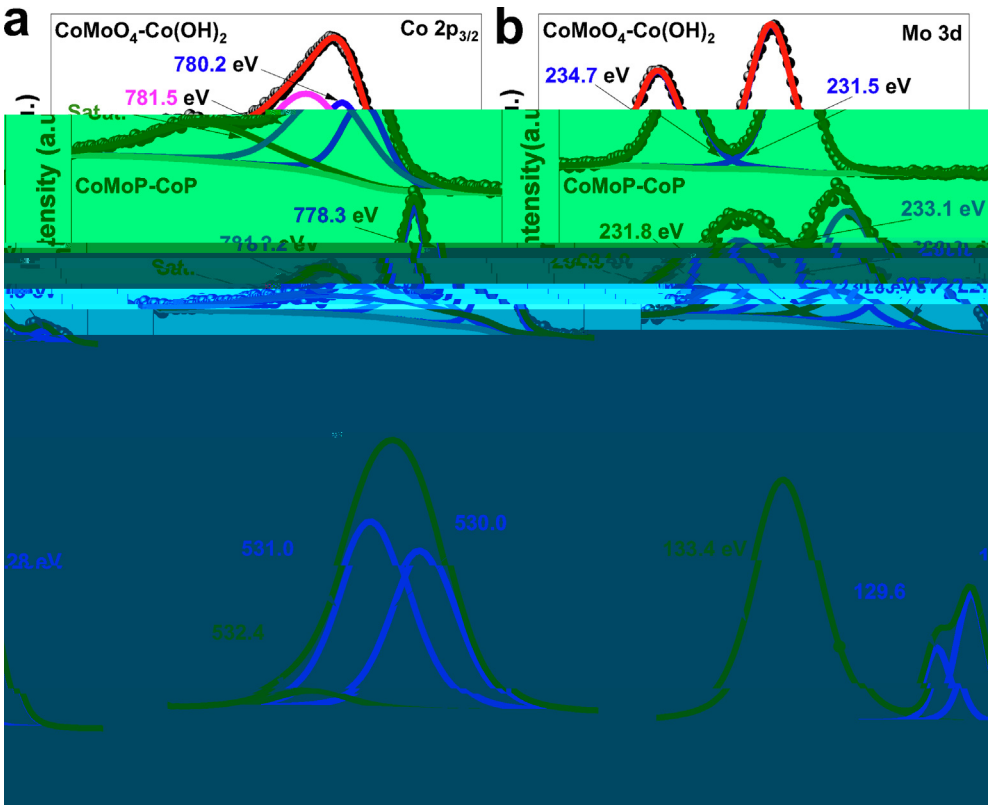

Fig. 4 – The XPS of (a) Co $2p_{3/2}$, (b) Mo 3*d* for CoMoP–CoP and $CoMoO_4$–$Co(OH)_2$, (c) O 1*s* for $CoMoO_4$–$Co(OH)_2$, (d) P 2*p* for CoMoP–CoP.

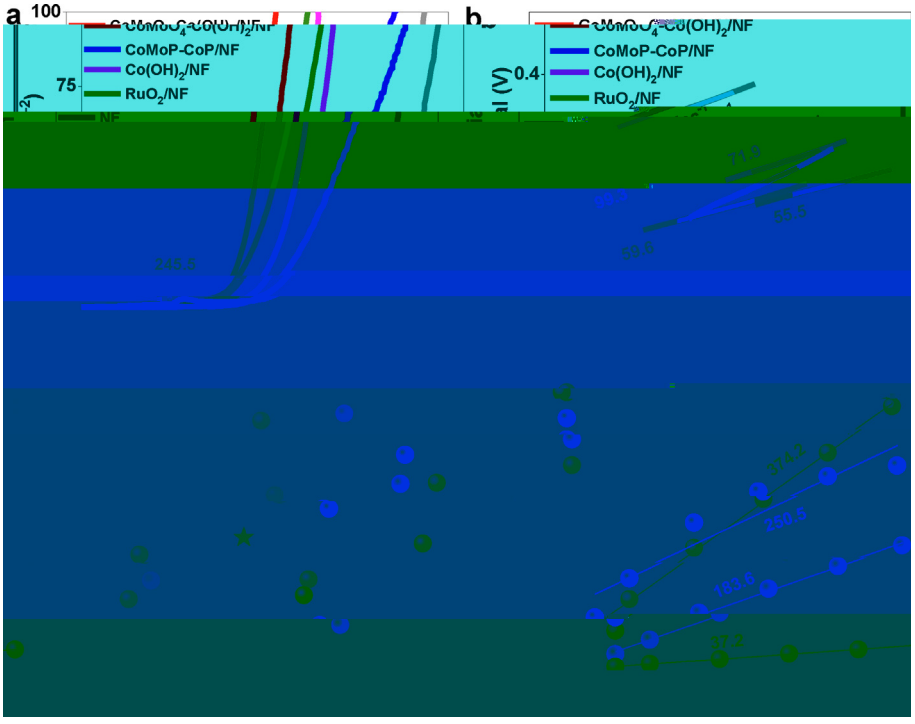

Fig. 5 – (a) Polarization curves of NF, RuO_2/NF, $Co(OH)_2$/NF, CoMoP–CoP/NF and $CoMoO_4$–$Co(OH)_2$/NF. (b) Tafel slope of corresponding OER. (c) Comparison of OER performance between $CoMoO_4$–$Co(OH)_2$/NF and similar published catalysts (Table S1). (d) C_{dl} diagram summarized by the CV curves of different voltage scan rates.

CoMoP–CoP/NF may follow by Volmer-Heyrovsky pathway [51], which suggests that electrochemical desorption is the rate determining step [52]. As we expected, the optimized $CoMoO_4$–$Co(OH)_2$/NF was designed as an OER catalyst, which showed a relatively low HER activity reflecting as high overpotential and Tafel slope. CoMoP–CoP/NF exhibits smaller semicircular diameters than that of CoP/NF, showing it has faster charge transfer ability (Fig. S8b). For $CoMoO_4$–$Co(OH)_2$/NF and CoMoP–CoP/NF catalyst, average relative deviations of voltage are below or equal to 2.0% at 10 mA cm^{-2}

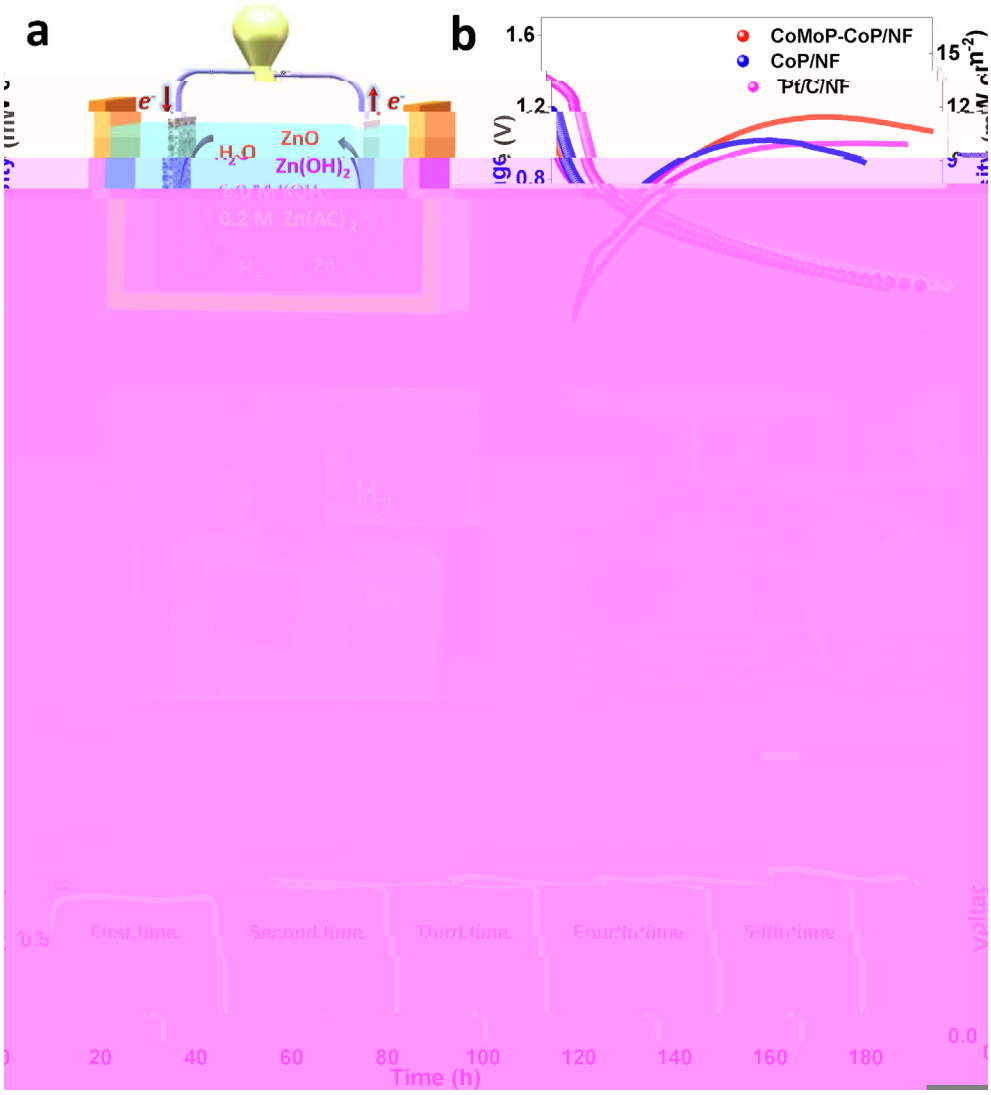

Fig. 7 – (a) Schematic diagram of the Zn–H_2O cell. (b) Polarization and power density curves about CoMoP–CoP/NF, CoP/NF and Pt/C. (c) Hydrogen bubbles produced on the cathode surface of CoMoP–CoP/NF. (d) Picture of one red LED light lit by two Zn–H_2O cell of CoMoP–CoP/NF. (e) Discharge curves of CoMoP–CoP/NF. The electrolyte in Fig. 7a–e is 6.0 M KOH and 0.2 M $Zn(AC)_2$.

Conclusions

In summary, the $CoMoO_4$–$Co(OH)_2$/NF and CoMoP–CoP/NF combined catalysts for water splitting and Zn–H_2O cell have successfully prepared via a two-step approach of - . conversion and phosphorization. The experimental results fully proved their multi-functional, robust and stable catalytic activities derived from the hierarchical structure, array-like sheets, fast charge transfer and synergistic effect. The combination of two catalysts could achieve highly stable water splitting at high current density used in industrial condition, and the resurrection of CoMoP–CoP/NF realized the repeated and stable operation of the same Zn–H_2O cell. We believe that the novel multifunctional non-noble metal-based catalysts has a bright future of realizing hydrogen production with lower energy consumption.

Declaration of competing interest

The authors declare that they have no known competing financial interests or personal relationships that could have appeared to influence the work reported in this paper.

Acknowledgements

This work has been supported by the National Natural Science Foundation of China (no. 21965005), Natural Science Foundation of Guangxi Province (2020GXNSFBA297001, 2021GX NSFAA076001), Guangxi Key Laboratory of Information Materials (201028-Z), Project of High-Level Talents of Guangxi (F-KA18015) and Guangxi Technology Base and Talent Subject (GUIKE AD18126001, GUIKE AD20297039).

Appendix A. Supplementary data

Supplementary data to this article can be found online at doi:10.1016/j.ijhydene.2022.05.136.

REFERENCES

[1] Zhou Y, Wang Z, Pan Z, Liu L, Xi J, Luo X, et al. Exceptional performance of hierarchical Ni-Fe (hydr)oxide@NiCu electrocatalysts for water splitting. Adv Mater 2019;31:1806769.

[2] Liu Z, Yuan C, Teng F. Crystal facets-predominated oxygen evolution reaction activity of earth abundant $CoMoO_4$ electrocatalyst. J Alloys Compd 2019;781:460–6.

[3] Li C, Zhang B, Li Y, Hao S, Cao X, Yang G, et al. Self-assembled Cu-Ni bimetal oxide 3D in-plane epitaxial structures for highly efficient oxygen evolution reaction. Appl Catal B Environ 2019;244:56–62.

[4] Li D, Liu D, Zhao S, Lu S, Ma Y, Li M, et al. Tuning of metallic valence in CoMoP for promoting electrocatalytic hydrogen evolution. Int J Hydrogen Energy 2019;44:31072–81.

[5] Kou Z, Zhang L, Ma Y, Liu X, Zang W, Zhang J, et al. 2D carbide nanomeshes and their assembling into 3D microflowers for efficient water splitting. Appl Catal B Environ 2019;243:678–85.

[6] Prematuri R, Turjaman M, Sato T, Tawaraya K. The impact of nickel mining on soil properties and growth of two fast-growing tropical trees species. Int J Res 2020;2020:8837590.

[7] Cao L-M, Lu D, Zhong D-C, Lu T-B. Prussian blue analogues and their derived nanomaterials for electrocatalytic water splitting. Coord Chem Rev 2020;407:213156.

[8] Kou T, Wang S, Hauser JL, Chen M, Oliver SRJ, Ye Y, et al. Ni foam-supported Fe-doped β-$Ni(OH)_2$ nanosheets show ultralow overpotential for oxygen evolution reaction. ACS Energy Lett 2019;4:622–8.

[9] Xun S, Xu Y, He J, Jiang D, Yang R, Li D, et al. MOF-derived cobalt oxides nanoparticles anchored on $CoMoO_4$ as a highly active electrocatalyst for oxygen evolution reaction. J Alloys Compd 2019;806:1097–104.

[10] Wang Y-Q, Zhao L, Sui X-L, Gu D-M, Wang Z-B. Hierarchical CoP_3/$NiMoO_4$ heterostructures on Ni foam as an efficient bifunctional electrocatalyst for overall water splitting. Ceram Int 2019;45:17128–36.

[11] Anandhababu G, Huang Y, Babu DD, Wu M, Wang Y. Oriented growth of ZIF-67 to derive 2D porous CoPO nanosheets for electrochemical-/photovoltage-driven overall water splitting. Adv Funct Mater 2018;28:1706120.

[12] Hu H-S, Li Y, Shao Y-R, Li K-X, Deng G, Wang C-B, et al. NiCoP nanorod arrays as high-performance bifunctional electrocatalyst for overall water splitting at high current densities. J Power Sources 2021;484:229269.

[13] Odynets IV, Strutynska NY, Li J, Han W, Zatovsky IV, Klyui NI. $CoO_x(OH)_y$/C nanocomposites in situ derived from $Na_4Co_3(PO_4)_2P_2O_7$ as sustainable electrocatalysts for water splitting. Dalton Trans 2018;47:15703–13.

[14] Yan P, Huang M, Wang B, ZixiaWan, Qian M, Yan H, et al. Oxygen defect-rich double-layer hierarchical porous Co_3O_4 arrays as high-efficient oxygen evolution catalyst for overall water splitting. J Energy Chem 2020;47:299–306.

[15] Chen M, Wang N, Wang X, Zhou Y, Zhu L. Enhanced degradation of tetrabromobisphenol A by magnetic Fe_3O_4@ZIF-67 composites as a heterogeneous Fenton-like catalyst. Chem Eng J 2020:127539.

[16] Lin D, Duan P, Yang W, Liu Y, Pan Q. Facile controlled synthesis of core–shell/yolk–shell/hollow ZIF-67@Co-LDH/SiO_2 via a self-template method. Inorg Chem Front 2020;7:1643–50.

[17] Ghoshal S, Zaccarine S, Anderson GC, Martinez MB, Hurst KE, Pylypenko S, et al. ZIF 67 based highly active electrocatalysts as oxygen electrodes in water electrolyzer. ACS Appl Energy Mater 2019;2:5568–76.

[18] Bao Y, Liu P, Zhang J, Wang L, Wang M, Mei H, et al. Construction of carbon quantum dots embed α-$Co/Ni(OH)_2$ hollow nanocages with enhanced supercapacitor performance. J Am Ceram Soc 2020;103:4342–51.

[19] Chuong ND, Thanh TD, Kim NH, Lee JH. Hierarchical heterostructures of ultrasmall Fe_2O_3-encapsulated MoS_2/N-graphene as an effective catalyst for oxygen reduction reaction. ACS Appl Mater Interfaces 2018;10:24523–32.

[20] Cheng X, Dou S, Qin G, Wang B, Yan P, Isimjan TT, et al. Rational design of highly selective nitrogen-doped Fe_2O_3-CNTs catalyst towards H_2O_2 generation in alkaline media. Int J Hydrogen Energy 2020;45:6128–37.

[21] Zha Q, Xu W, Li X, Ni Y. Chlorine-doped α-$Co(OH)_2$ hollow nano-dodecahedrons prepared by a ZIF-67 self-sacrificing template route and enhanced OER catalytic activity. Dalton Trans 2019;48:12127–36.

[22] Li H, Zhao X, Liu H, Chen S, Yang X, Lv C, et al. Sub-1.5 nm ultrathin CoP nanosheet aerogel: efficient electrocatalyst for hydrogen evolution reaction at all pH values. Small 2018;14:1802824.

[23] Dang Y, He J, Wu T, Yu L, Kerns P, Wen L, et al. Constructing bifunctional 3D holey and ultrathin CoP nanosheets for efficient overall water splitting. ACS Appl Mater Interfaces 2019;11:29879–87.

[24] Liu Z, Zhan C, Peng L, Cao Y, Chen Y, Ding S, et al. A $CoMoO_4$-$Co_2Mo_3O_8$ heterostructure with valence-rich molybdenum for a high-performance hydrogen evolution reaction in alkaline solution. J Mater Chem 2019;7:16761–9.

[25] Jia D, Gao H, Xing L, Chen X, Dong W, Huang X, et al. 3D self-supported porous NiO@$NiMoO_4$ core-shell nanosheets for highly efficient oxygen evolution reaction. Inorg Chem 2019;58:6758–64.

[26] Jiang D, Xu Y, Yang R, Li D, Meng S, Chen M. CoP_3/CoMoP heterogeneous nanosheet arrays as robust electrocatalyst for pH-universal hydrogen evolution reaction. ACS Sustainable Chem Eng 2019;7:9309–17.

[27] Liu B, Li H, Cao B, Jiang J, Gao R, Zhang J. Few layered N, P dual-doped carbon-encapsulated ultrafine MoP nanocrystal/MoP cluster hybrids on carbon cloth: an ultrahigh active and durable 3D self-supported integrated electrode for hydrogen evolution reaction in a wide pH range. Adv Funct Mater 2018;28:1801527.

[28] Gan Q, Cheng X, Chen J, Wang D, Wang B, Tian J, et al. Temperature effect on crystallinity and chemical states of nickel hydroxide as alternative superior catalyst for urea electrooxidation. Electrochim Acta 2019;301:47–54.

[29] Tao K, Dan H, Hai Y, Liu L, Gong Y. Controllable synthesis of MoO linkage enhanced CoP ultrathin nanosheet arrays for efficient overall water splitting. Appl Surf Sci 2019;493:852–61.

[30] Xu Y, Xie L, Li D, Yang R, Jiang D, Chen M. Engineering $Ni(OH)_2$ nanosheet on $CoMoO_4$ nanoplate Array as efficient electrocatalyst for oxygen evolution reaction. ACS Sustainable Chem Eng 2018;6:16086–95.

[31] Yu H, Qi L, Hu Y, Qu Y, Yan P, Isimjan TT, et al. Nanowire-structured FeP-CoP arrays as highly active and stable bifunctional electrocatalyst synergistically promoting high-current overall water splitting. J Colloid Interface Sci 2021;600:811–9.

[32] Thangavel P, Kim G, Kim KS. Electrochemical integration of amorphous NiFe (oxy)hydroxides on surface-activated carbon fibers for high-efficiency oxygen evolution in alkaline

anion exchange membrane water electrolysis. J Mater Chem 2021;9:14043–51.
[33] Harzandi AM, Shadman S, Nissimagoudar AS, Kim DY, Lim H-D, Lee JH, et al. Ruthenium core–shell engineering with nickel single atoms for selective oxygen evolution via nondestructive mechanism. Adv Energy Mater 2021;11:2003448.
[34] Thangavel P, Ha M, Kumaraguru S, Meena A, Singh AN, Harzandi AM, et al. Graphene-nanoplatelets-supported NiFe-MOF: high-efficiency and ultra-stable oxygen electrodes for sustained alkaline anion exchange membrane water electrolysis. Energy Environ Sci 2020;13:3447–58.
[35] Lyu F, Bai Y, Li Z, Xu W, Wang Q, Mao J, et al. Self-templated fabrication of CoO-MoO_2 nanocages for enhanced oxygen evolution. Adv Funct Mater 2017;27:1702324.
[36] Zhang S, She G, Li S, Qu F, Mu L, Shi W. Enhancing the electrocatalytic activity of $NiMoO_4$ through a post-phosphorization process for oxygen evolution reaction. Catal Commun 2019;129:105725.
[37] An L, Feng J, Zhang Y, Wang R, Liu H, Wang G-C, et al. Epitaxial heterogeneous interfaces on N-$NiMoO_4$/NiS_2 nanowires/nanosheets to boost hydrogen and oxygen production for overall water splitting. Adv Funct Mater 2019;29:1805298.
[38] Dou Y, Zhang L, Xu J, He C-T, Xu X, Sun Z, et al. Manipulating the architecture of atomically thin transition metal (hydr) oxides for enhanced oxygen evolution catalysis. ACS Nano 2018;12:1878–86.
[39] Wang H, Li Y, Wang R, He B, Gong Y. Metal-organic-framework template-derived hierarchical porous CoP arrays for energy-saving overall water splitting. Electrochim Acta 2018;284:504–12.
[40] Han X, Yu C, Huang H, Guo W, Zhao C, Huang H, et al. Phase controllable synthesis of Ni^{2+} post-modified CoP nanowire for enhanced oxygen evolution. Nano Energy 2019;62:136–43.
[41] Du X, Che P, Wang Y, Yuan C, Zhang X. Ni_3S_2@$Co(OH)_2$ heterostructures grown on Ni foam as an efficient electrocatalyst for water oxidation. Int J Hydrogen Energy 2019;44:22955–61.
[42] Li Y, Wang C, Cui M, Chen S, Ma T. A novel strategy to synthesize $CoMoO_4$ nanotube as highly efficient oxygen evolution reaction electrocatalyst. Catal Commun 2019;131:105800.
[43] Jin YZ, Li Z, Wang JQ, Li R, Li ZQ, Liu H, et al. Tuning spin state of rock-salt-based oxides by manipulation of crystallinity for efficient oxygen electrocatalysis. Adv Energy Mater 2018;8:1703469.
[44] Wang F, Zhao J, Tian W, Hu Z, Lv X, Zhang H, et al. Morphology-controlled synthesis of $CoMoO_4$ nanoarchitectures anchored on carbon cloth for high-efficiency oxygen oxidation reaction. RSC Adv 2019;9:1562–9.
[45] Wang X, Rong F, Huang F, He P, Yang Y, Tang J, et al. Facile synthesis of hierarchical $CoMoO_4$@$Ni(OH)_2$ core-shell nanotubes for bifunctional supercapacitors and oxygen electrocatalysts. J Alloys Compd 2019;789:684–92.
[46] Wang P, Liu X, Yan Y, Cao J, Feng J, Qi J. Exploring CoP core-shell nanosheets by Fe and Zn dual cation doping as efficient electrocatalysts for overall water splitting. Catal Sci Technol 2020;10:1395–400.
[47] Feng Y, Xu C, Hu E, Xia B, Ning J, Zheng C, et al. Construction of hierarchical FeP/Ni_2P hollow nanospindles for efficient oxygen evolution. J Mater Chem 2018;6:14103–11.
[48] Yang F, Chen X, Li Z, Wang D, Liu L, Ye J. Ultrathin FeP nanosheets as an efficient catalyst for electrocatalytic water oxidation: promoted intermediates adsorption by surface defects. ACS Appl Energy Mater 2020;3:3577–85.
[49] Zhong J, Wu T, Wu Q, Du S, Chen D, Chen B, et al. N- and S-co-doped graphene sheet-encapsulated Co_9S_8 nanomaterials as excellent electrocatalysts for the oxygen evolution reaction. J Power Sources 2019;417:90–8.
[50] Wang M, Fu W, Du L, Wei Y, Rao P, Wei L, et al. Surface engineering by doping manganese into cobalt phosphide towards highly efficient bifunctional HER and OER electrocatalysis. Appl Surf Sci 2020;515:146059.
[51] Li Y, Jiang Z, Huang J, Zhang X, Chen J. Template-synthesis and electrochemical properties of urchin-like NiCoP electrocatalyst for hydrogen evolution reaction. Electrochim Acta 2017;249:301–7.
[52] Ma Y-Y, Wu C-X, Feng X-J, Tan H-Q, Yan L-K, Liu Y, et al. Highly efficient hydrogen evolution from seawater by a low-cost and stable CoMoP@C electrocatalyst superior to Pt/C. Energy Environ Sci 2017;10:788–98.
[53] Meng C, Lin M, Sun X, Chen X, Chen X, Du X, et al. Laser synthesis of oxygen vacancy-modified CoOOH for highly efficient oxygen evolution. ChemComm 2019;55:2904–7.
[54] Chi K, Tian X, Wang Q, Zhang Z, Zhang X, Zhang Y, et al. Oxygen vacancies engineered $CoMoO_4$ nanosheet arrays as efficient bifunctional electrocatalysts for overall water splitting. J Catal 2020;381:44–52.
[55] Wang L, Huang Z, Huang H, Zhong S, Huang M, Isimjan TT, et al. Electron-transfer enhanced sponge-like CrP-Re_2P as a robust bifunctional electrocatalyst for high-current overall water splitting and Zn–H_2O cell. Electrochim Acta 2022;404:139598.
[56] Liu Y-C, Koza JA, Switzer JA. Conversion of electrodeposited $Co(OH)_2$ to CoOOH and Co_3O_4, and comparison of their catalytic activity for the oxygen evolution reaction. Electrochim Acta 2014;140:359–65.
[57] Zhou H, Yu F, Zhu Q, Sun J, Qin F, Yu L, et al. Water splitting by electrolysis at high current densities under 1.6 volts. Energy Environ Sci 2018;11:2858–64.
[58] Wang B, Huang H, Sun T, Yan P, Isimjan TT, Tian J, et al. Dissolution reconstruction of electron-transfer enhanced hierarchical NiS_x-MoO_2 nanosponges as a promising industrialized hydrogen evolution catalyst beyond Pt/C. J Colloid Interface Sci 2020;567:339–46.